AGU PUBLICATIONS

JGR

Journal of Geophysical Research: Space Physics

RESEARCH ARTICLE

10.1002/2013JA019221

Key Points:
- O+ is dominant heavy species escaping Mars
- High-altitude O+ drives high- and low-energy distributions not seen in heavies
- High- and low-energy O+ may not be detected and heavies/O can be overestimated

Correspondence to:
S. M. Curry,
smcurry@umich.edu

Citation:
Curry, S. M., M. Liemohn, X. Fang, Y. Ma, J. Slavin, J. Espley, S. Bougher, and C. F. Dong (2014), Test particle comparison of heavy atomic and molecular ion distributions at Mars, *J. Geophys. Res. Space Physics*, *119*, 2328–2344, doi:10.1002/2013JA019221.

Received 12 JUL 2013
Accepted 26 FEB 2014
Accepted article online 4 MAR 2014
Published online 31 MAR 2014

Test particle comparison of heavy atomic and molecular ion distributions at Mars

S. M. Curry[1], M. Liemohn[1], X. Fang[2], Y. Ma[3], J. Slavin[1], J. Espley[4], S. Bougher[1], and C. F. Dong[1]

[1]Department of Atmospheric and Space Sciences, University of Michigan, Ann Arbor, Michigan, USA, [2]Laboratory for Atmospheric and Space Physics, University of Colorado Boulder, Boulder, Colorado, USA, [3]Institute of Geophysics and Planetary Physics, University of California, Los Angeles, California, USA, [4]NASA Goddard Space Flight Center, Greenbelt, Maryland, USA

Abstract This study uses the Mars Test Particle simulation to create virtual detections of O^+, O_2^+, and CO_2^+ in an orbital configuration in the Mars space environment. These atomic and molecular planetary pickup ions are formed when the solar wind directly interacts with the neutral atmosphere, causing the ions to be accelerated by the background convective electric field. The subsequent ion escape is the subject of great interest, specifically with respect to which species dominates ion loss from Mars. O^+ is found to be the dominant escaping ion because of the large sources of transported ions in the low-energy (<10 eV) and high-energy (>1 keV) range. O_2^+ and CO_2^+ are observed at these energy ranges but with much lower fluxes and are generally only found in the tail between 10 eV and 1 keV. Using individual particle traces, we reveal the origin and trajectories of the low-energy downtail O^+ populations and high-energy polar O^+ populations that contribute to the total escape. Comparing them against O_2^+ and CO_2^+ reveals that the extended hot oxygen corona contributes to source regions of high- and low-energy escaping ions. Additionally, we present results for solar minimum and maximum conditions with respect to ion fluxes and energies in order to robustly describe the physical processes controlling planetary ion distributions and atmospheric escape.

1. Introduction

Unmagnetized planets are especially susceptible to atmospheric scavenging, so the distribution and escape of heavy ion species serve as important indicators for the evolution of atmospheric volatiles. Without the presence of an intrinsic dipole magnetic field, individual ion motion is dictated by the direct interaction of the solar wind with the upper neutral atmosphere. Mars has a weaker gravitational field than Earth ($G_M \sim 38\%\ G_E$) so when ions are newly created, especially at high altitudes, they can readily be picked up and accelerated away by the convective electric field with gyroradii on the planetary scale size.

To address the role that these ions have in the evolution of atmospheric volatiles and their inventories, numerous modeling efforts and observations have posed the question of which species dominates the mass loss at Mars. Multispecies [*Ma et al.*, 2004; *Ma and Nagy*, 2007; *Manning et al.*, 2011] and some hybrid studies [*Modolo et al.*, 2005] concluded that O^+ is the most dominant escaping ion in terms of number flux. Using a test particle approach, *Yagi et al.* [2012] also found that the high-altitude hot component of O dominated the nonthermal escape flux and that O^+ was the dominant escaping ion species by examining the seasonal and local variations of the thermal exosphere components O, CO, CO_2, and O_2. Yet multifluid [*Najib et al.*, 2011] and other hybrid [*Kallio et al.*, 2010] modeling studies concluded that O_2^+ has the larger total loss rate.

Observational studies using the Ion Mass Analyzer (IMA) of the Analyzer of Space Plasmas and Energetic Atoms (ASPERA-3) instrument package on Mars Express (MEX) have found that O^+ is the most dominant escaping ion [*Barabash et al.*, 2007; *Lundin et al.*, 2009; *Nilsson et al.*, 2011]. But mass separation by the IMA is less reliable for heavier species, especially at higher energies, because the ion composition is derived by fitting the ion mass peak as a function of energy and mass to Gaussian peaks [*Barabash et al.*, 2007]. Prior to 2007, the IMA lower energy threshold was 30 eV, which also limited the heavy ion sampling. In addition to the complexity of resolving the mass of these ions, the total IMA angular coverage is 90° from the viewing plane but parts of the field of view are blocked by the spacecraft and solar wind panels [*Nilsson et al.*, 2012]. Because of these limitations, the question of how the heavy ion species (CO_2^+, O_2^+, and O^+) are transported and observed in the Mars space environment remains open.

A test particle approach is well suited to compare heavy pickup ions at Mars because it can account for the effects of extremely large gyroradii on the scale of the planetary radius. While test particle models are not self-consistent, they can be used to address questions surrounding the removal of oxygen from Mars' atmosphere by utilizing billions of particles to get a macroscopic representation of ion distributions in near Mars space. Previous test particle studies at Mars include *Luhmann and Schwingenschuh* [1990] and *Luhmann and Kozyra* [1991] who examined the influence of O^+ precipitation and escape on sputtering and nonthermal escape processes. Test particle modeling was also employed by *Leblanc and Johnson* [2002] and *Cipriani et al.* [2007] in order to explore the nonthermal sources of hot O, C, CO_2, and CO in the Martian exosphere, again in the context of sputtering of atomic O. *Chaufray et al.* [2007] examined global maps of escape, sputtering and dissociative recombination (DR) of O^+ using a test particle simulation and suggested DR played an important role for producing nonthermal oxygen. *Fang et al.* [2008, 2010a, 2010b] also investigated the factors influencing escaping O^+, including particle kinetic energy and the local time and presence of the crustal fields. Additionally, *Curry et al.* [2013b, 2013a] examined the effect of ion production mechanisms, solar conditions, and neutral atmospheric configurations on O^+ escape in the context of test particle modeling.

This paper is a study of the heavy ion transport and escape at Mars using a test particle simulation. Recent model developments have been tailored to study CO_2^+, O_2^+, and O^+ ion populations produced in the upper atmosphere of Mars. The paper begins with a discussion of the modeling approach and ion chemistry in section 2. Following, the results for each heavy ions species with energy-time spectrogram, velocity space, particle traces, and escape distributions are presented in section 3. Finally, section 4 presents a brief discussion of the results and concluding remarks.

2. Approach

The Mars Test Particle (MTP) simulation is a collisionless test particle simulation that follows the trajectories of particles of any atomic weight through the Mars space environment. Because the model is collisionless and not self-consistent, background fields for the bulk velocity, electric and magnetic field lines, and steady state low-altitude ions are necessary. The MTP uses the results based on the *Ma et al.* [2004] study at solar maximum, described below.

2.1. MHD Model

The 3-D multispecies MHD (MS-MHD) model, based on the *Ma et al.* [2004] study, employs four continuity, one momentum, one magnetic induction, and one energy equation. This iteration of the (C. Dong et al., Solar wind interaction with Mars upper atmosphere: Results from the one-way coupling between the multi-fluid MHD model and the MTGCM model, submitted to *Geophysical Research Letters*, 2014) model does not include the Hall or polarization electric fields and calculates the background convective electric field from $\mathbf{E} = -\mathbf{U} \times \mathbf{B}$. Crustal magnetic fields are implemented with a 60° spherical harmonic scheme from *Arkani-Hamed* [2001] and positioned to face the Sun at 180°W, 0°N. This is an important feature of the MHD model because these crustal magnetic regions were first observed [*Acuna et al.*, 1999] by the Mars Global Surveyor and have been found to significantly shield the planet from the direct interaction of the solar wind [*Fraenz et al.*, 2006; *Fang et al.*, 2010a; *Dubinin et al.*, 2011; *Lundin et al.*, 2011b].

The MHD model lower boundary is set at 100 km above the Martian surface, where the O^+, O_2^+, and CO_2^+ densities are taken to be the photochemical equilibrium values [*Bougher and Engel*, 2000] and the H^+ density is set to be approximately zero. The model adopts a nonuniform, spherical grid structure with a radial resolution varying from 10 km at the lower boundary to 630 km at the outer boundary (~20 Mars radii) and with angular resolution varying from 1.875° to 3.75°. The computational domain is defined by $-24\ R_M \leq X \leq 8\ R_M$; $-16\ R_M \leq Y, Z \leq 16\ R_M$, where R_M is the radius of Mars (~ 3396 km). A reflective inner boundary condition for the velocity $\mathbf{u}$ (perpendicular flow) is used, which results in near zero velocity at the inner boundary as expected. The plasma temperature at the inner boundary is set to be twice the value of the neutral temperature, and the upstream solar wind plasma temperatures were set to 3.5×10^5 K. The interplanetary magnetic field (IMF) was assumed to be a Parker spiral in the *X*-*Y* plane with an angle of 56° (away sector) with a field strength of 3 nT, where the solar wind velocity and density were set at 400 km/s and 4 cm^{-3}. Figure 1 illustrates the *XZ* plane of the steady state solution for the magnetic field and bulk flow velocity (Figures 1 (top) and 1 (bottom), respectively).

The multispecies MHD model has been one-way coupled with the Mars Thermospheric Global Circulation Model (M-TGCM) developed by *Bougher and Engel* [2000], *Bougher et al.* [2006], and (C. Dong et al.,

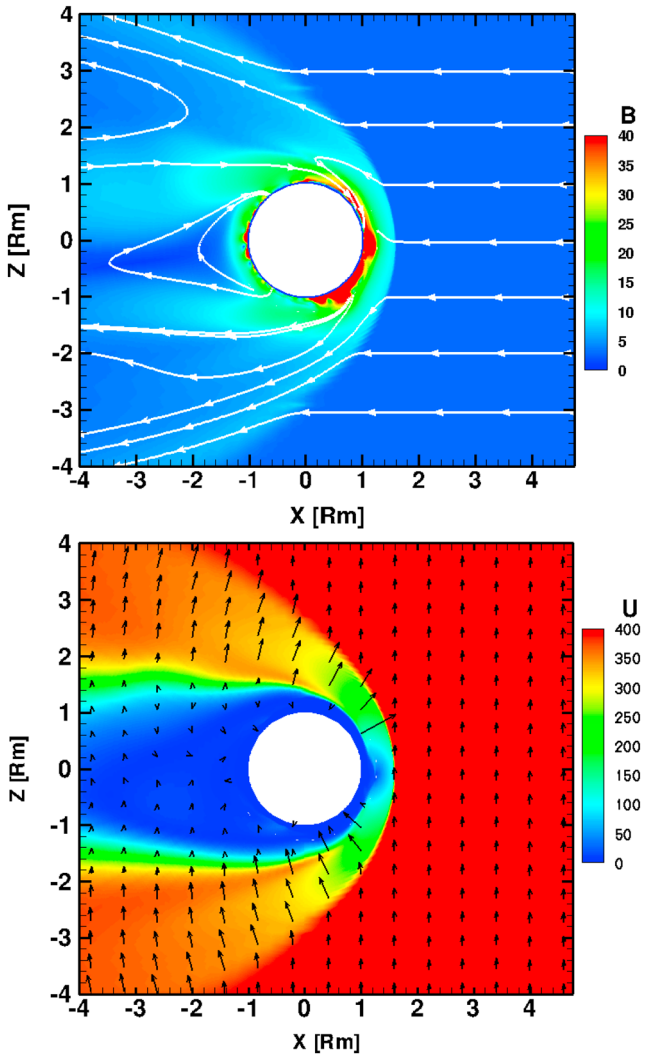

Figure 1. The background MHD (top) magnetic field and (bottom) bulk velocity in the *XZ* (meridian) plane. The color bars show the magnitudes in nT and km/s, respectively; the white lines marked with arrows indicate the vector direction of the magnetic field and the black arrows show the electric field direction and magnitude.

submitted manuscript, 2014) and used to investigate the corresponding ion escape rates [*Ma and Nagy*, 2007]. The M-TGCM predicts significant variations of the density and temperature with solar zenith angle, as well as solar cycle; the model is constrained by observations from MGS (Mars Global Surveyor), Mars Odyssey, and MRO (Mars Reconnaissance Orbiter). The modern M-TGCM code contains equations for the major neutral species (CO_2, CO, N_2, and O), selected minor neutral species (Ar, NO, N(^4S), and O_2), and several photochemically produced ions (O_2^+, CO_2^+, O^+, CO^+, and NO^+). The resolution in latitude and longitude is 5°, and the vertical coordinate is log pressure with a resolution equaling to 0.5 scale heights. The hot oxygen atom densities are adopted from *Kim et al.* [1998], which are assumed to be spherically symmetric. Figure 2 illustrates the neutral densities and ion production rates at 300 km as a function of local time and latitude. It should be noted that the neutral O density has a strong peak on the nightside at 200 km [*Bougher and Engel*, 2000; *Valeille et al.*, 2009b] but since the simulation begins at 300 km, the peak has shifted poleward.

2.2. Mars Test Particle Simulation

The main approach for this study is a 3-D Monte Carlo model that randomly assigns the particles' initial position, energy, and direction within each cell of a spherical grid around Mars. The simulation begins with initialization of the atmosphere and ion production, discussed in depth in section 2.3. The MTP currently uses the neutral atmospheric profile from the background MS-MHD model, where O and CO_2 are the main constituents.

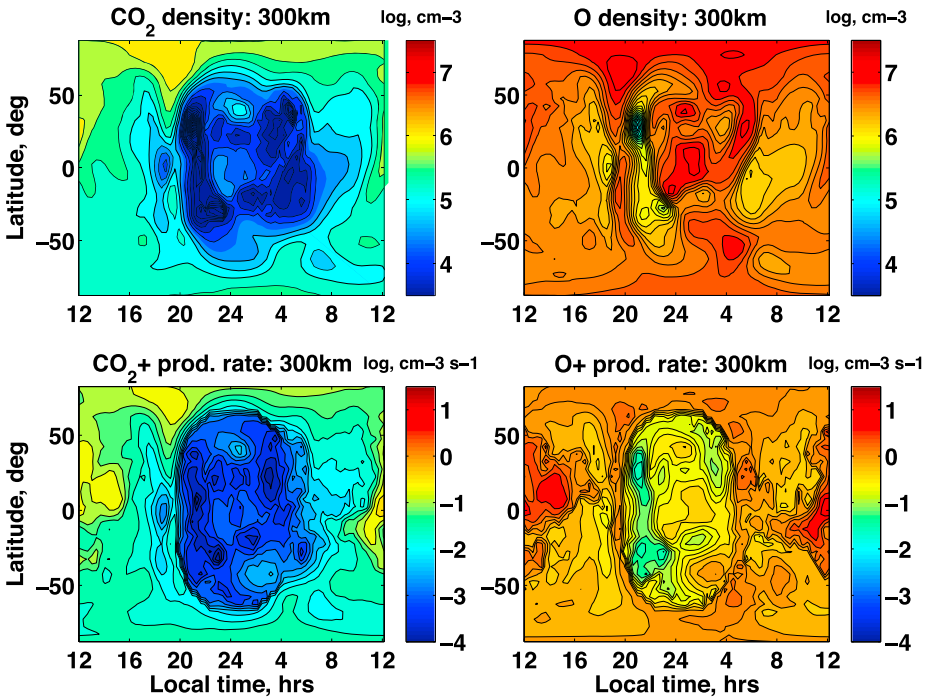

Figure 2. (top) The neutral densities for (left) CO_2 and (right) O at 300 km (cm^{-3}, log). (bottom) The ion production rates for CO_2^+ and O^+ at 300 km (cm^{-3} s^{-1}, log).

The neutral temperature is provided by M-TGCM [*Bougher et al.*, 2006, 2008] and the initial energy and velocity distribution for the particles is a Maxwellian centered on this neutral temperature. It should be noted that 2 eV is added to the initial energy which *Fang et al.* [2010b] suggested may be due to partially reflective of different initial ion heating [*Ergun et al.*, 2006]. This artificial energy has been used by *Luhmann and Schwingenschuh* [1990], *Kallio* [2002], *Fang et al.* [2008], and *Curry et al.* [2013b, 2013a] and manifests itself as a 2 eV peak in ion fluxes but does not change the overall energy distribution because the electromagnetic fields control the ion escape as opposed to gravity (the gravitational binding energy at 200 km is roughly 2 eV) [*Fang et al.*, 2010b].

After initialization, the model launched 4.5 billion particles (15,000 particles per source cell) time-independently in order to create high-resolution velocity space distributions. Recall the central limit theorem that states that the relative error in counting statistics is proportional to one over the square root of the number of counts. Thus, in order to achieve density within 10% accuracy, each measurement location requires 100 particles contributing to this quantity. Because the MTP simulation is well suited to resolve small-scale features in velocity space, each cell needs extremely high accuracy in regions of interest in velocity space. However, due to the weighting of the particles, the total ion escape rate converges with only 50 to 100 particles per source cell. Because of the finite gyroradius effects, the escape will slightly diverge from the background MHD model but should be in relative agreement.

Once the particles are launched, the particles are considered collisionless. This places a limit on the inner boundary to stand above the Martian exobase, which *Fox* [2009] and *Valeille et al.* [2010] estimated to be 180–250 km for solar minimum and maximum cases. Loss sources due to collisions of ions with the ambient neutrals are subsequently assumed to be negligible. The inner boundary in this simulation is 300 km and extends out to 4 R_M.

The MTP simulation uses a spherical grid and cells with 5° by 5° resolution. The grid cells are logarithmically spaced with respect to radial distance [*Fang et al.*, 2008]. A Cartesian coordinate system corresponding to the Mars Solar Orbital (MSO) scheme is adopted where the system is centered at Mars and X_{MSO} points toward the Sun, Y_{MSO} is aligned with the dusk direction, and Z_{MSO} completes the right-hand system. Because the IMF is a Parker spiral in the ecliptic plane away from the Sun in this simulation, the MSO and

Mars–Sun– Electric field (where Z_{MSE} is aligned with the interplanetary electric field) coordinate systems are equivalent for this case.

Each particle is accelerated by the background electric and magnetic field and travels until it reaches the inner boundary or the outer boundary where the positions and trajectories are recorded. A sophisticated parallelization scheme was developed by *Fang et al.* [2008] in order to support the taxing computational requirements. Each particle carries a weight determined by the ion production per unit time per cell divided by the total number of test particles [*Fang et al.*, 2008]. The trajectory is determined by solving Newton's equation of motion where the pickup ion transport is dictated by the Lorentz force and gravity. The MTP solves for the velocity and position of the particle using a staggered leap frog scheme at half time steps, where one time step is 0.05 s. The velocity is stepped using the Boris scheme implemented by *Birdsall and Langdon* [1985] and *Fang et al.* [2008]. The total acceleration on each particle is a half step acceleration by the electric field ($t-1/2$), a rotation in the perpendicular plane to the magnetic field, and then a half step acceleration by the electric field ($t+1/2$). Each step includes gravity so the individual ion motion combines a gyration around the magnetic field, the $\mathbf{E} \times \mathbf{B}$ drift, and the gravitational force toward the planet (equations (2)–(4)).

$$\frac{d\mathbf{v}}{dt} = \frac{q}{m_s}(\mathbf{E} + \mathbf{v} \times \mathbf{B}) - G\hat{\mathbf{r}} \tag{1}$$

$$\mathbf{v}^{-} = \mathbf{v}^{t-\frac{1}{2}} + \frac{\Delta t}{2}\frac{q}{m_s}\mathbf{E}^{t} - \frac{\Delta t}{2}\frac{GM_m}{r^2}\hat{\mathbf{r}} \tag{2}$$

$$\mathbf{v}^{+} - \mathbf{v}^{-} = \frac{q}{m_s}\frac{\mathbf{v}^{+} + \mathbf{v}^{-}}{2}\Delta t \times \mathbf{B} \tag{3}$$

$$\mathbf{v}^{+} = \mathbf{v}^{t+\frac{1}{2}} - \frac{\Delta t}{2}\frac{q}{m_s}\mathbf{E}^{t} - \frac{\Delta t}{2}\frac{GM_m}{r^2}\hat{\mathbf{r}} \tag{4}$$

where $\mathbf{v}$ is the velocity vector, q is the electric charge, m_s is the mass of the species, $\mathbf{E}$ is the convective electric field, $\mathbf{B}$ is the magnetic field, G is the universal gravitational constant, $\hat{\mathbf{r}}$ is the unit radial vector, and M_m is the mass of Mars. A particle travels until it reaches the inner boundary of 300 km or the outer boundary of 4 R_M.

The MTP simulation tracks the full angular distribution of the particles by placing virtual detectors around the planet with no implicit averaging of the gyration or pitch angle of the particles. Once the particles' trajectory and velocity are recorded, velocity space distributions can be constructed. In this study, 410 virtual detectors are aligned in an orbital configuration based on the June 2007 MEX orbit no. 4438.

2.3. Ion Production Schemes

The reaction rates included in this simulation are based on *Bougher and Engel* [2000], *Schunk and Nagy* [2000], *Fox and Sung* [2001], *Ma et al.* [2004], and *Curry et al.* [2013b], which are listed in Table 1. Molecular nitrogen and helium were not included because their neutral density profiles are comparatively small above 300 km. Additionally, dissociative recombination was not included for any source because the MTP simulation follows only ion species and the neutral atmosphere is assumed to be in equilibrium. Three physical processes are included for ion production: photoionization, charge exchange, and electron impact.

The first process for ion production is photoionization without solar zenith angle dependence, as seen in equation (5). X represents any of the neutrals that will be ionized and traced throughout the simulation (O, O_2, or CO_2). This ionization process uses a constant reaction rate except in the cylindrical optical shadow behind the planet (the nightside) because the simulation has a lower boundary of 300 km, where the atmosphere is already optically thin. The photoionization factor, f, is therefore 1 everywhere except this optical shadow, where it would be 0.

$$X + h\nu \rightarrow X^{+} + e^{-}$$

$$k_1 = f \times \text{constant}(X)(\text{s}^{-1}) \tag{5}$$

The charge exchange process, described at length in *Curry et al.* [2013b], includes two types of reactions for planetary neutrals interacting with an ion : (1) charge exchange between a neutral species and solar wind protons and (2) charge exchange between a neutral species and a planetary ion (the species are again

Table 1. Chemical Reaction Rates

Chemical Reaction	Rate Coefficient ($cm^3\ s^{-1}$)	Reference
$CO_2 + h\nu \rightarrow CO_2^+ + e$	$f = 7.30 \times 10^{-7}\ s^{-1}$	*Schunk and Nagy* [2000]
$CO_2 + h\nu \rightarrow O^+ + CO + e$	$f = 7.40 \times 10^{-8}\ s^{-1}$	*Schunk and Nagy* [2000]
$O + h\nu \rightarrow O^+ + e$	$f = 2.73 \times 10^{-7}\ s^{-1}$	*Schunk and Nagy* [2000]
$H + h\nu \rightarrow H^+ + e$	$f = 8.59 \times 10^{-8}\ s^{-1}$	*Ma et al.* [2004]
$CO_2^+ + O \rightarrow CO_2 + O^+$	$k = 9.60 \times 10^{-11}$	*Schunk and Nagy* [2000]
$H^+ + O \rightarrow H + O^+$	$k = v_{total}\ (1{\times}10^{-15})$	*Curry et al.* [2013b][a]
$H^+ + CO_2 \rightarrow H + CO_2^+$	$k = v_{total}\ (2{\times}10^{-15})$	*Curry et al.* [2013b][a]
$O^+ + H \rightarrow O + H^+$	$k = 6.40 \times 10^{-10}$	*Fox and Sung* [2001]
$CO_2^+ + H \rightarrow CO_2 + H^+$	$k = 2.35 \times 10^{-11}$	*Fox and Sung* [2001]
$H^+ + H \rightarrow H + H^+$	$k = v_{total}\ (2.5{\times}10^{-15})$	*Curry et al.* [2013b][a]
$H^+ + O_2 \rightarrow H + O_2^+$	$k = v_{total}\ (2{\times}10^{-15})$	*Curry et al.* [2013b][a]
$CO_2^+ + O \rightarrow CO + O_2^+$	$k = 1.64 \times 10^{-10}$	*Fox and Sung* [2001]
$CO_2^+ + O_2 \rightarrow CO_2 + O_2^+$	$k = 5.50 \times 10^{-11}(300/T_i)^{0.82}$ for $T_i \leq 1500$ K $1.50 \times 10^{-11}(T_i/1500)^{0.75}$ for $T_i > 1500$ K	*Fox and Sung* [2001]
$O^+ + O_2 \rightarrow O + O_2^+$	$k = 1.60 \times 10^{-11}(300/T_i)^{0.52}$ for $T_i \leq 900$ K $9.00 \times 10^{-12}(T/900)^{0.92}$ for $T_i > 900$ K	*Fox and Sung* [2001]
$O^+ + CO_2 \rightarrow CO + O_2^+$	$k = 1.10 \times 10^{-9}$ for $T_i \leq 800$ K $1.10 \times 10^{-9}(T_i/800)^{-0.39}$ for $T_i > 800$ K	*Fox and Sung* [2001]
$CO_2 + e \rightarrow O^+ + e + e$	table lookup	*Cravens et al.* [1987]
$O + e \rightarrow O^+ + e + e$	table lookup	*Cravens et al.* [1987]
$H + e \rightarrow O^+ + e + e$	table lookup	*Cravens et al.* [1987]

[a]Charge exchange using bulk and thermal velocity (hot neutrals).
[b]*Martinis et al.* [2003] versus *Fox and Sung* [2001].

denoted by X). The first type of charge exchange describes how the neutrals in the corona will experience collisions with the solar wind protons. This reaction rate (k_{2a}, cm^3/s) accounts for the change in the bulk velocity as the solar wind approaches the planetary obstacle where energy is transferred to the particle's thermal velocity. The reaction rate can be described by multiplying the $H^+ - X$ cross section, σ, by the total velocity, v_{total}, in each cell. Equations (6)–(9) denote the total velocity as the combination of the bulk velocity and the thermal velocity. T_i is assumed to be half the plasma temperature and thus is assumed to be equivalent to T_e from the MHD results. Charge exchange between planetary protons and neutral species has been neglected but has been previously explored by *Kallio et al.* [2007, 2008].

The second charge exchange rate (k_{2b}, cm^3/s) characterizes the collision between an ion and a cold planetary neutral species. For example, the reaction $CO_2^+ + O \rightarrow CO_2 + O^+$ is when a planetary CO_2^+ ion and O coronal atom exchange an electron and can be described with a constant, nontemperature-dependent reaction rate of $9.60 \times 10^{-11}\ cm^{-3}\ s^{-1}$.

$$X + H_{SW}^+ \rightarrow X^+ + H_{SW}$$

$$v_{thermal} = \sqrt{\frac{2kT_i}{m}} \tag{6}$$

$$v_{bulk} = \sqrt{U_x^2 + U_y^2 + U_z^2} \tag{7}$$

$$v_{total} = \sqrt{v_{thermal}^2 + v_{bulk}^2} \tag{8}$$

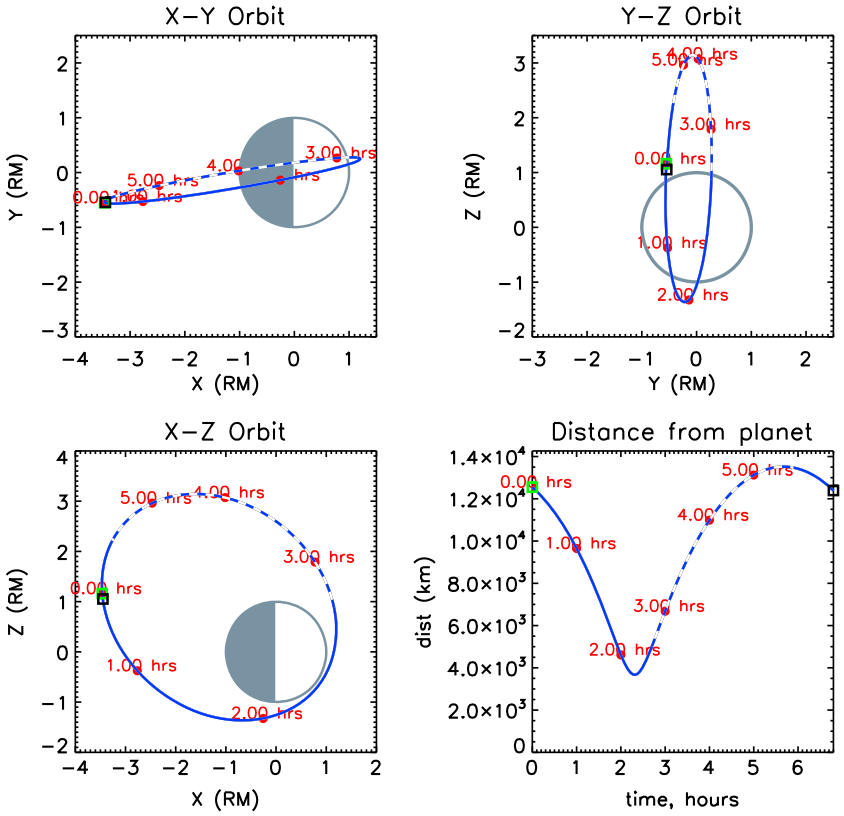

Figure 3. The orbit of the virtual detectors which are placed inside of the MTP simulation. The planes are the (left top) *XY*, (left bottom) *XZ*, and (right top) *YZ* planes in units of R_M. (right bottom) The distance from the planets in kilometers. The red time stamps denote the location of the virtual detectors during the orbit. The green square denotes the beginning of the orbit and the black square denotes the end. The blue dashed sector of the orbit denotes when it is in the induced magnetosheath region.

$$k_{2a} = v_{\text{total}} \times \sigma(\text{cm}^3\text{s}^{-1}) \tag{9}$$

$$X_1 + X_2^+ \rightarrow X_1^+ + X_2$$

$$k_{2b} = \text{constant}(X)(\text{cm}^3\text{s}^{-1}) \tag{10}$$

The final ionization process is electron impact ionization, which uses electron temperature (T_e) dependent rates based on the schema for impact ionization from *Cravens et al.* [1987], as seen in equation (11).

$$X + e^- \rightarrow X^+ + e^- + e^-$$

$$k_3 = F_C(T_e)(\text{cm}^3\text{s}^{-1}) \tag{11}$$

2.4. Ionospheric Source

In addition to the three ionization processes discussed above, an additional source of ions is included in the simulation: ionospheric outflow [*Liemohn et al.*, 2013]. The MTP simulation does not include the ionosphere due to the inner boundary at 300 km, but the MHD model used for the background fields begins at 100 km and uses 10 km grid resolution. Thus, the upward flux at 300 km in the MHD simulation represents the ionospheric outflow from 100 to 300 km. This method has also been employed by *Modolo et al.* [2005], *Kallio et al.* [2010], and *Liemohn et al.* [2013].

This flux is injected into the MTP simulation at 300 km and treated as a fourth ion source carrying its own weighting per particle. The particles launched as the ionospheric outflow source have an initial energy with a Maxwellian now at the local ion temperature (where $T_i = 1/2\ T_p$) as opposed to a Maxwellian at the neutral temperature. Their initial velocity is also that of the local bulk velocity.

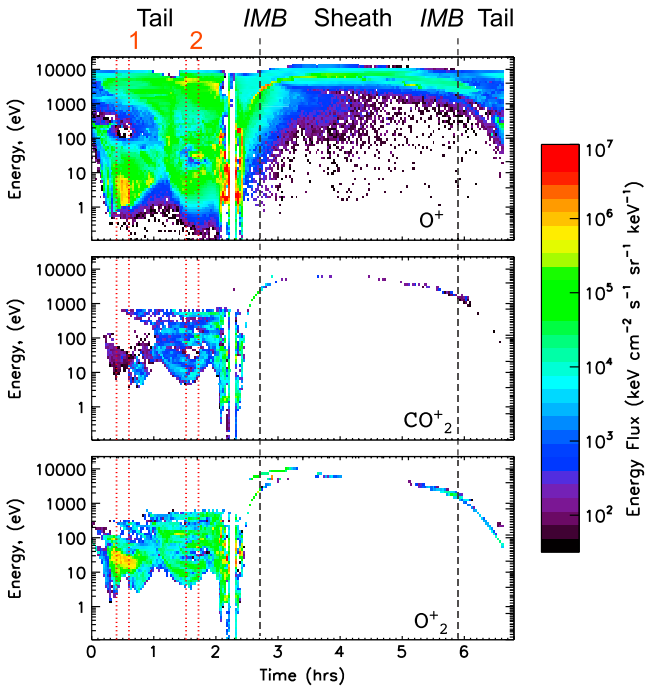

Figure 4. An energy-time spectrogram of (top) O^+, (middle) CO_2^+, and (bottom) O_2^+ are plotted as a function of differential energy flux (keV cm^{-2} s^{-1} sr^{-1} keV^{-1}) for time versus energy. The IMB, which separates the sheath from the tail region, was estimated by *Lundin et al.* [2011a] and is marked with dashed black lines. The red dotted lines around 0.5 h and 1.6 h signify two regions of interest that will be discussed in the following sections.

In summary, particles in the simulation represent ions created from each of the aforementioned sources. Each particle is weighted, where we define weight as the number of ions represented by a test particle. This is determined by the ion production from photoionization, charge exchange, electron impact, and ionospheric outflow in each cell divided by the total number of test particles per unit time.

3. Results

3.1. Energy Time Spectrograms

The MTP simulation traced the ion trajectories of O^+, CO_2^+, and O_2^+ and recorded the energy and flight direction of each particle that passed through virtual detectors placed in an orbit around Mars. The orbit corresponds to MEX orbit no. 4438 and is roughly 6.5 h, and the detector moves counterclockwise around the planet in the *XZ* plane if the Sun is to the right. Figure 3 illustrates the orbit configuration of the virtual detectors in the *XY*, *XZ*, and *YZ* planes as well as the distance from the planet (km). The orbit begins in the tail region and passes near the south pole of the planet as it approaches periapsis at 2.4 h. The detector then passes across the induced magnetic boundary (IMB) at 2.7 h and into the sheath region from roughly 2.7–5.9 h, which is marked with the dashed lines. Finally, the detector crosses back over the IMB at 5.9 h and into the tail region again from 5.9 to 6.5 h.

Figure 4 shows an energy-time spectrogram (ETS) that was constructed using the measurements from the virtual detectors and describes the response of the pickup ions to the $\mathbf{E} \times \mathbf{B}$ drift in Mars plasma environment [*Hartle et al.*, 2011]. O^+, CO_2^+, and O_2^+ are plotted in Figures 4 (top), 4 (middle), and 4 (bottom), respectively, as a function of differential energy flux (keV cm^{-2} s^{-1} sr^{-1} keV^{-1}) for time versus energy. The IMB separates the sheath from the tail region and is marked with the dashed black lines estimated using MEX data by *Lundin et al.* [2011a]. The dotted red lines denote two areas of interest that will be further expanded upon in velocity space and particle traces in Figures 5–9. While the entire orbit has interesting features, we focus on the tail because the magnetosheath is relatively uniform in velocity space and energy.

By examining the orbit from the beginning in Figure 4, the highest fluxes can be seen in the tail from 0 to 2.4 h (tail to periapsis). It is immediately evident that the O^+ ions are observed at all energy ranges, especially above 1 keV, and that the regions with the high flux occur at periapsis around 2.4 h. While the CO_2^+

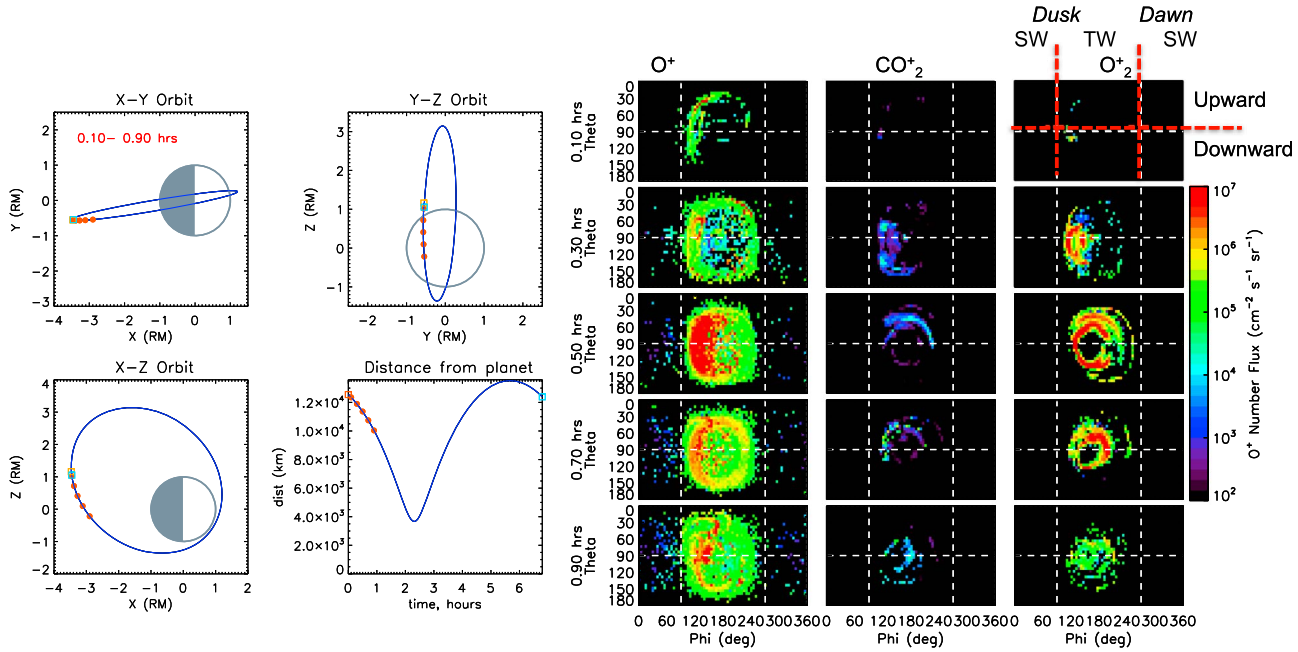

Figure 5. (left) An illustration of where the virtual detector was in the orbit with a red dot in the *XY*, *XZ*, and *YZ* planes (in R_M) from 0.1 to 0.9 h in the energy-time spectrogram. (right) Velocity space distributions for (top) O^+, (middle) CO_2^+, and (bottom) O_2^+ are plotted and labeled for each location from 0.1 to 0.9 h. The velocity space distributions illustrate the ions integrated from 0 to 25 keV.

and O_2^+ ions peak at periapsis as well, they are observed in much narrower energy ranges and with much lower fluxes.

As the detector moves into the dayside region and toward apoapsis from 2.4 to 5.9 h, all three species exhibit high-energy populations above 1 keV, particularly as the detector crosses the IMB and enters into the induced sheath region at ~2.7 h (dashed black lines). The detectors in the sheath, the region denoted in Figure 3 by the dashed blue and white line, observe high-energy ions from 1 to 10 keV because the convective electric field is accelerating them tailward and upward ($-X_{MSO}$, $+Z_{MSO}$). Finally, the detector reaches apoapsis at roughly 5.6 h and enters back into the tail region at 5.9 h. As the detector enters the tail, the observed ions lose energy and approach 100 eV again.

3.2. Tailward Ion Transport

The velocity distribution function at a given point in the orbit is an important indicator of (1) the details of ion transport and escape at that location and (2) how different ion species are accelerated between their source and observation locations. The first area of interest in the orbit corresponds to 0.1–0.9 h in the tail region, designated by the red dotted lines in Figure 4 labeled "1," which Figures 5–6 will expand on.

Figure 5 illustrates the detectors, represented with red dots along the orbit in Figure 5 (left), with the corresponding velocity space distributions (VSDs) of O^+, CO_2^+ and O_2^+ in Figure 5 (right). Beginning with the general trends in the downtail transport of the ions, the virtual detector moves through an area of high-flux ions, peaking at roughly 0.5 h. Initially, at 0.1–0.3 h, the detector observes lower fluxes and then observes an increase in flux for all species at 0.5 h. Note that the virtual detector is still above the equatorial plane ($Z_{MSO} > 0$) and observes peak fluxes here because the convective electric field points upward and tailward ($+Z_{MSO}$, $-X_{MSO}$), which transports ions from the southern hemisphere upward and tailward into to the northern hemisphere. As the detector approaches $Z_{MSO} = 0$ and passes through the equatorial plane (0.7–0.9 h), the observed flux decreases.

The VSDs in Figure 5 also illustrate a clear trend in the flux of different ion species. The O^+ dominates the flux downtail with counts from 10^5 to 10^7 cm^{-2} s^{-1} sr^{-1}. The CO_2^+ ions contribute the least flux, which is 3 orders of magnitude lower at 10^3–10^4 cm^{-2} s^{-1} sr^{-1}, but has VSD signatures that closely resemble O_2^+. This similarity in the CO_2^+ and O_2^+ signatures is a result of the lower altitude, cold neutral source of the ions (≤500 km), and heavier atomic mass. The oxygen species on the other hand has a hot neutral corona due to

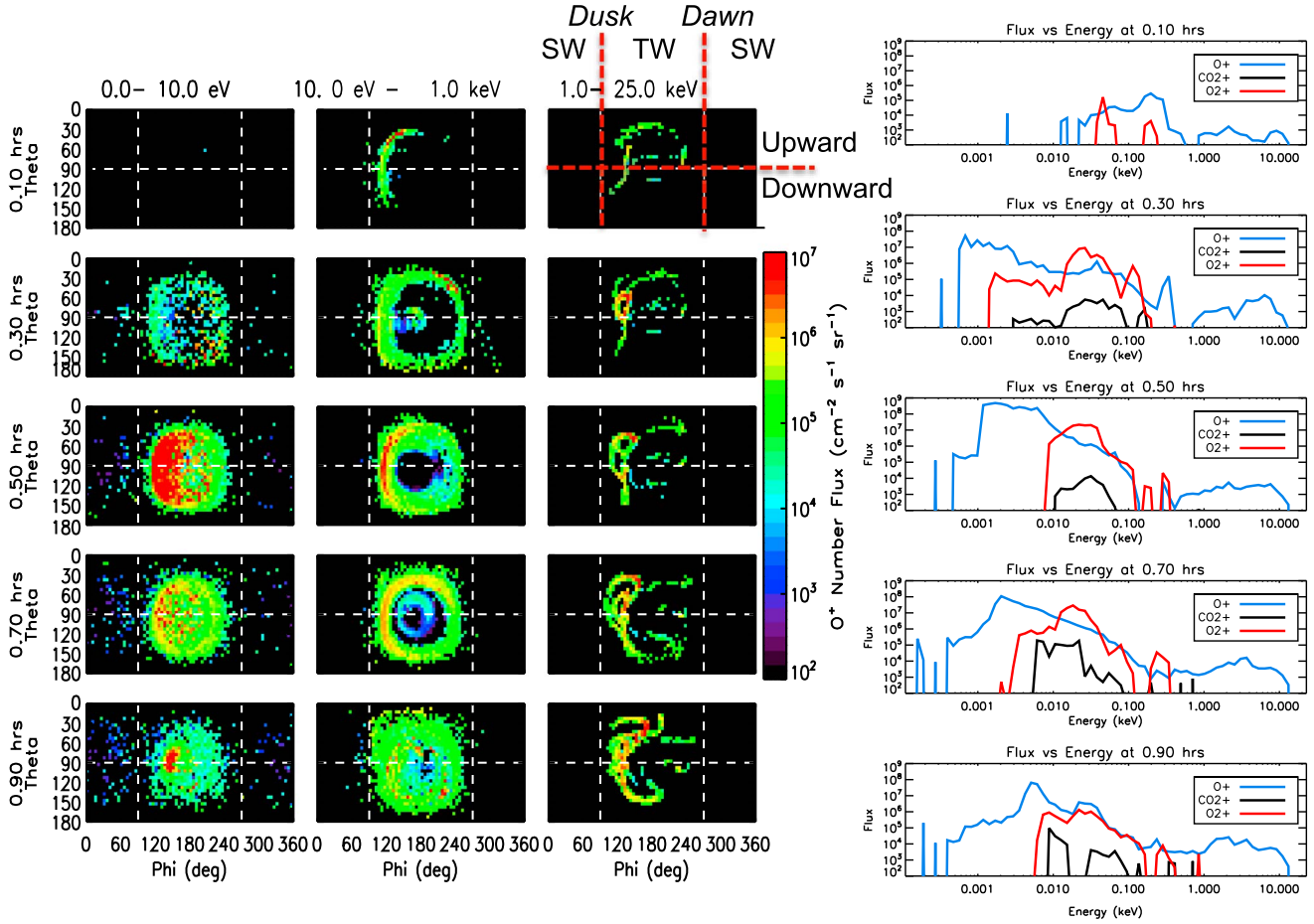

Figure 6. (left) An illustration of O^+ velocity space distributions downtail from 0.1 to 0.9 h for three energy ranges: low: 0–10 eV, medium: 10 eV to 1 keV, and high: 1–25 keV. (right) An illustration of the flux versus energy signatures O^+, CO_2^+, and O_2^+ at the same locations.

dissociative recombination and sputtering [*Fox and Hac*, 1997; *Nagy et al.*, 2004; *Chaufray et al.*, 2007; *Cipriani et al.*, 2007; *Barabash and Holmstrom*, 2002; *Valeille et al.*, 2009a] which gives it a high-altitude source of O^+ (≥500 km). This hot oxygen corona at Mars plays an important role in the VSDs, as discussed in depth by *Curry et al.* [2013a].

While each species exhibits the trend of a flux peak as the detector moves through the tail, the velocity space signatures vary. Because the ions are accelerated tailward, most of the downtail VSD signatures have a flight direction centered around $\phi = 180°$ and $\theta = 90°$, but each species has distinct asymmetries. O^+ is detected at a much broader range of flight directions, which is to say that O^+ has much more flight direction coverage than the heavier planetary species. We adopt the phrase *flight direction coverage* to describe how much flux the detector observes across all angles (i.e., how much or little empty space there is for a given virtual detection). The broad range flight direction coverage in O^+ is especially visible at 0.5 h with enhanced flux at a flight direction near dusk, $\phi = 90–180°$. *Kallio et al.* [2007] observed the same patterns downtail in a hybrid study of O^+ and O_2^+ and attributed the larger flight direction coverage in O^+ to the extended oxygen corona. In addition to flight direction asymmetries, the energy ranges are distinct. Referring back to Figure 4 at 0.5 h (the first area of interest marked in dotted red lines), the ETS illustrates the O^+ flux peaks between 1 and 10 eV while O_2^+ peaks between 10 and 100 eV.

Figure 6 expands on the low-energy, high-flux O^+ by illustrating the O^+ velocity space integrated over three energy ranges (low: 0–10 eV, medium: 10 eV to 1 keV, and high: 1–25 keV) in Figure 6 (left) and the flux as a function of energy for O^+, CO_2^+, and O_2^+ at 0.1–0.9 h in Figure 6 (right). From 0.3 to 0.7 h, the detector observes large fluxes of low-energy ions: 1–2 eV for O^+ and 11–12 eV for CO_2^+ and O_2^+. A critical result is this low-energy O^+ flux, which dominates the energy spectrum. At 0.5 h, the total integrated O^+ and O_2^+ flux

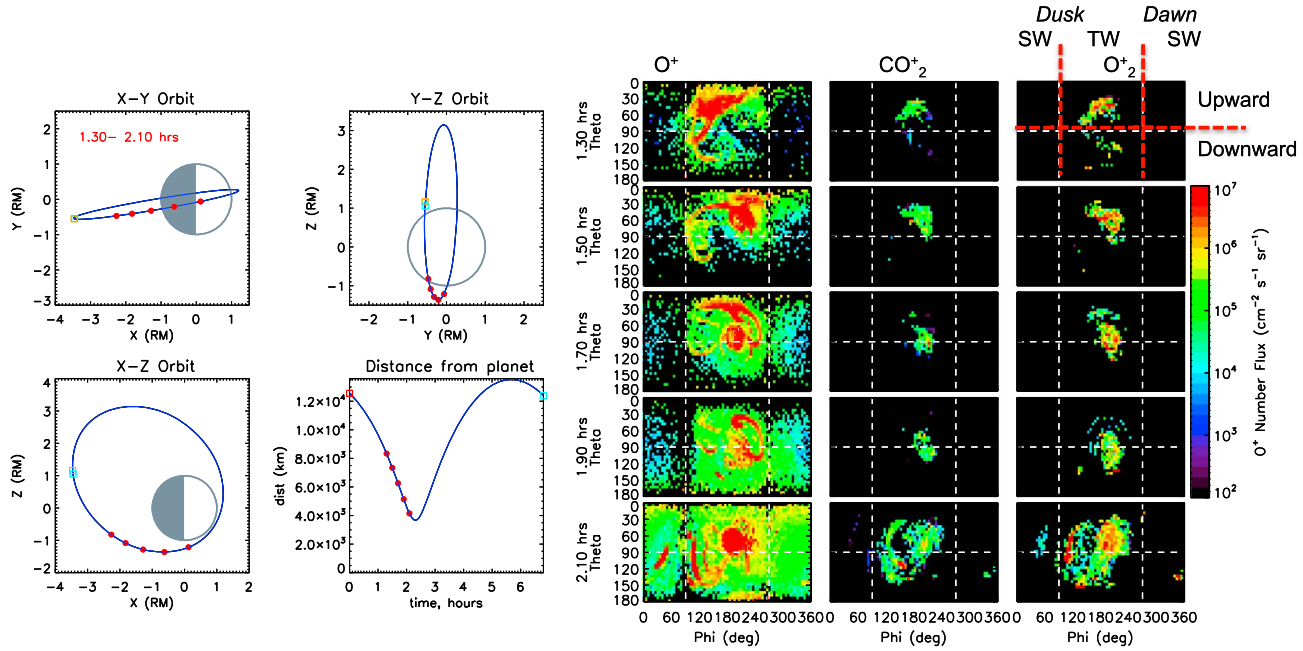

Figure 7. (left) An illustration where the virtual detector was in the orbit with a red dot in the *XY*, *XZ*, and *YZ* planes (in R_M) from 1.3–2.1 h in the energy-time spectrogram. (right) Velocity space distributions for (top) O^+, (middle) CO_2^+, and (bottom) O_2^+ are plotted and labeled for each location from 1.3 to 2.1 h. The velocity space distributions illustrate the ions integrated from 0 to 25 keV.

at the detector is 3.3×10^9 and 1.2×10^8 cm^{-2} s^{-1}, respectively, which indicates that O^+ is dominant by over an order of magnitude. Note that at roughly 7 eV, the O_2^+ flux becomes dominant; this is an important distinction with upcoming missions such as Mars Atmosphere and Volatile Evolution (MAVEN) that will be investigating the escape rates of different ion species over a range of energies.

The detector has the most coverage at 0.5 h because the electric field is both upward and tailward. In the *XZ* plane shown in Figure 5, the detector moves from the *+Z* plane to the *−Z* plane (crossing the equatorial plane). At 0.5 h, the detector is aligned to observe the ions being accelerated from the southern pole up to the equatorial plane. The detector at 0.3 h observes fewer ions because the ions being accelerated from southern hemisphere precipitate into the planet first. As the detector approaches 0.9 h, ions have to originate from much farther away to be accelerated to this location so the cold, low-energy ions decrease and the high-energy ions increase, as seen in Figure 5 (left).

It should be noted that a data comparison is beyond the scope of this study especially because our away-sector Parker spiral configuration may not accurately reflect the conditions for this selected MEX orbit. MEX did not have a magnetometer, and thus, there is no information about the interplanetary magnetic field (IMF) configuration. Some studies have estimated the IMF clock angle from ion data upstream of the bow shock [*Yamauchi et al.*, 2007] or approximated from MGS during concurrent measurements. *Kallio et al.* [2006, 2008] used the latter method with MGS measurements in order to compare MEX energy-time spectrograms with a hybrid simulation of O^+ and O_2^+ but saw a number of differences which they attributed to a limited field of view. *Kallio et al.* [2007] also performed a similar study as the one presented here using a hybrid model and will be discussed further in the results. Future work will certainly include a comparison with data using an appropriate IMF configuration and will be well suited for comparisons with the Mars Atmosphere and Volatile Evolution (MAVEN) mission.

3.3. Polar Ion Transport

The second area of interest in the orbit corresponds to 1.3–2.1 h in the southern polar section of the orbit approaching periapsis, designated by the red dotted lines in Figure 4 labeled "2," which Figures 7–9 will expand on. This area highlights the role of ion transport and escape in regions with a much denser atmosphere. Figure 7 illustrates the detectors, represented with red dots along the orbit in Figure 7 (left), with the corresponding VSDs of O^+, CO_2^+ and O_2^+ in Figure 7 (right). As discussed in the previous section, the velocity

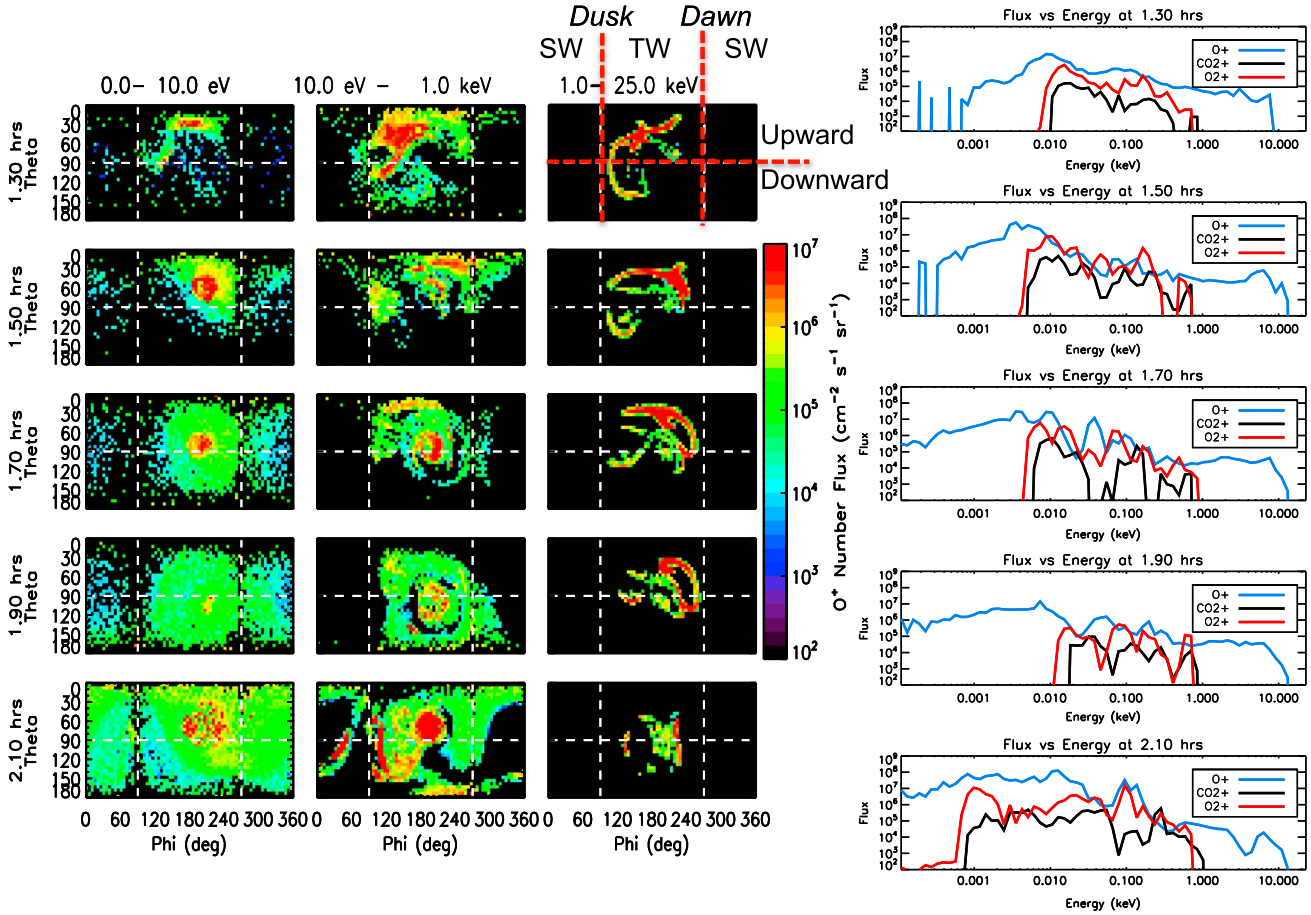

Figure 8. (left) An illustration of O^+ velocity space distributions illustrate from 1.3 to 2.1 h for three energy ranges: low: 0–10 eV, medium: 10 eV to 1 keV, and high: 1–25 keV. (right) An illustration of the flux versus energy signatures O^+, CO_2^+, and O_2^+ at the same locations.

space at a given time is indicative of how the planetary ions are being transported and how different species react to the **E** × **B** drift as a function of their finite gyroradius.

Figure 7 displays a clear trend of increasing flux and flight direction coverage as the detector approaches periapsis and moves closer to the planet. From 1.3 to 1.7 h, the flux remains constant for all three species even as the different flux populations change shape in velocity space. By 2.1 h, the detector is roughly 650 km from the surface resulting in all three species having high-flux concentrations above 10^7 cm^{-2} s^{-1} sr^{-1} and the detector having almost total flight direction coverage for O^+.

While the detectors in Figure 7 observe constantly increasing flux for each species, the detector observes very different velocity space signatures for O^+, CO_2^+, and O_2^+. The VSDs in the southern pole are more focused and asymmetric than the VSDs from the downtail detections (Figures 5–6). The CO_2^+ and O_2^+ VSDs have beams of ions that have converged at $\theta \sim 90°$, $\phi \sim 180°$. Both species have asymmetric shapes and shift slightly dawnward flight ($180° < \phi < 270°$) by 2.1 h as they cross the terminator.

However, O^+ has the most distinct asymmetric features in velocity space at the southern pole. At 1.3 h, a strong duskward, high-flux population is forming with a filamental, beam-like structure. From 1.5 to 1.7 h, this O^+ population evolves into two high-flux populations: (1) a central beam with a flight direction moving tailward ($\phi = 180°$ and $\theta = 90°$), similar to its CO_2^+ and O_2^+ counterparts and (2) a filamental beam of ions moving upward and arcing across $90° < \phi < 270°$ and $30° < \theta < 60°$. At 1.9 h, this high-flux filamental structure dominates with an upward, dawnward flight direction and much more flight direction coverage. Finally, at 2.1 h, the detector is flying through the hot oxygen corona and almost saturates the detector in flight direction coverage. The CO_2^+ and O_2^+ also have higher flux and more flight direction coverage at 2.1 h, but with specific focused populations of high-flux moving mostly downtail.

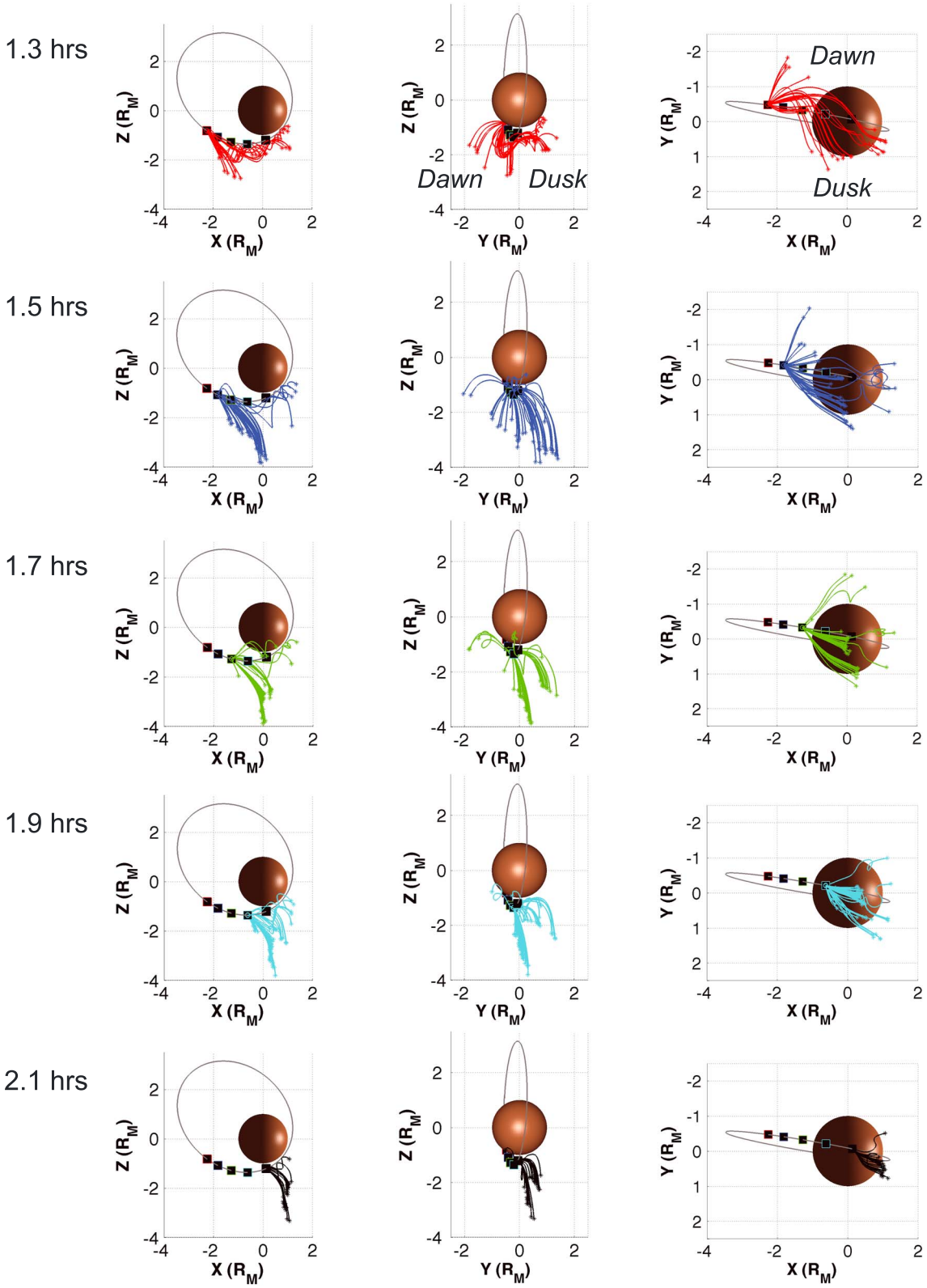

Figure 9. Particle trajectories of O^+ with an energy above 1 keV at each detector from 1.3–2.1 h. (left column) The trajectories of just for a profile view (*XZ* plane; Sun to the right), (middle column) the trajectories of O^+ face on in the *YZ* plane. (right column) An illustration of the O^+ particles from a bottom view, looking up at the south pole (*XY* plane; Sun to the right).

Table 2. O^+, CO_2^+, and O_2^+ Loss Rates (s^{-1})

Species	Inner Loss	Outer Loss	Efficiency
Solar Maximum			
O^+	5.0×10^{24}	4.3×10^{24}	46.1%
CO_2^+	8.6×10^{23}	1.3×10^{23}	13.1%
O_2^+	8.4×10^{24}	1.1×10^{24}	11.6%
Total	1.4×10^{25}	5.5×10^{24}	27.9%
Solar Minimum			
O^+	6.6×10^{23}	4.5×10^{23}	40.4%
CO_2^+	2.0×10^{23}	3.0×10^{22}	13.0%
O_2^+	8.5×10^{23}	1.1×10^{23}	11.4%
Total	1.7×10^{24}	5.9×10^{23}	25.6%

In Figure 8, we highlight these distinct ion populations as function of their energy at 1.3–2.1 h. Figure 8 (left) displays the O^+ velocity space integrated over three energy ranges (low: 0–10 eV, medium: 10 eV to 1 keV, and high: 1–25 keV) followed by the flux as a function of energy for O^+, CO_2^+, and O_2^+ in Figure 8 (right). In Figure 8 (left), the low-energy range is similar to the downtail velocity space signatures, but the middle- and high-energy ranges consist of asymmetric O^+ filamental structures spanning across various flight directions. These filamental structures show that O^+ is moving mostly upward in a highly nongyrotropic manner and the origins of these filamental structures will be further expanded on in Figure 9.

Figure 8 (right) illustrates the flux as a function of energy for O^+, CO_2^+, and O_2^+ from 1.3 to 2.1 h. As discussed in the previous plot, the flux increases as the detector approaches periapsis at 2.1 h, and the O^+ flux is responsible for the majority of the flight direction coverage. The CO_2^+ and O_2^+ are confined to the low to middle 10 eV to 1 keV range until the detector approaches 2.1 h, and it observes enhanced low-energy flux (< 10 eV) for each species. This low-energy flux corresponds to the cold planetary ions, which have previously been modeled and observed [*Lundin et al.*, 2009; *Terada et al.*, 2009]. But the lack of the high-energy CO_2^+ and O_2^+ ions contributes to the relatively symmetric velocity space distribution. Comparing the high-energy flux in the south pole to the high-energy flux downtail (Figure 6), the higher energy flux in the southern pole is over an order of magnitude higher.

Now that Figures 7 and 8 have isolated the high-energy and high-flux O^+ population near the south pole, Figure 9 illustrates a particle trajectories of the O^+ ions that were observed above 1 keV at each detector. Vertically, the traces are from 1.3 to 2.1 h where Figure 9 (left column) is a profile view (*XZ*) of the high-energy O^+ origin and trajectories, Figure 9 (middle) is a front view (*YZ*) of the same system, and Figure 9 (right column) is a view from underneath the planet (*XY*). Again, it should be noted that particles originating closer to the detectors were observed but did not have energies above 1 keV and are not shown here. The particles in Figure 9 are accelerated in the $+E_{SW}$ direction into the detectors, each outlined in black, cyan, green, blue, and red.

Each view of these high-energy O^+ ions in Figure 9 shows specific trajectories so that the velocity space signatures in Figure 8 can be traced to specific origins. From 1.5 to 1.9 h in Figure 8, the VSDs show a dawnward high-flux, high-energy arcing beam. The corresponding detectors in Figure 9 show trajectories with a high number of particles at dusk (Figures 9 (middle) and 9 (right) where $Y_{MSO} > 0$) moving to the detector near $Y_{MSO} = 0$, thus having a dawnward flight direction. Additionally, detectors at 1.5–1.9 h observe the high-altitude O^+ sources originating from as far as 3–4 R_M below Mars. This is an important finding because CO_2^+ and O_2^+ do not have a high-altitude neutral source [*Bougher et al.*, 2004, 2008] and therefore cannot generate ions which are accelerated for long enough distances to reach >5 keV energies in the southern pole region. This is consistent with the velocity space signatures modeled by *Kallio et al.* [2007] showing a linear relation with distance from a detector and observed energy. Again, these results are for a specific IMF case; if the IMF was reversed, the convective electric field would also reverse and point downward ($-Z_{MSO}$), which in turn would make these ions from the southern hemisphere accelerating upward toward the planet now accelerate downward and away from the planet and escape.

3.4. Ratio of Ion Escape

Illustrated by the observed flux in the downtail and periapsis regions, O^+ dominates the loss rates on a 4 R_M shell, as seen by Table 2. The table includes the following parameters for each solar cycle: the species, the rate of ion precipitation into the atmosphere at the lower boundary (inner loss, s^{-1}), the rate of ion escape through the outer boundary (outer loss, s^{-1}), the efficiency (%). Efficiency is defined as the ratio of the outer loss to the total production of ions (or the sum of the inner and outer loss) and is a measure of the likelihood of escape.

At solar maximum, the O^+ outer loss is roughly 4 times larger than the heavy species (CO_2^+ and O_2^+) and has the highest efficiency of 46%. The ratio of the heavy species outer loss to O^+ outer loss is 0.29, where O_2^+ is

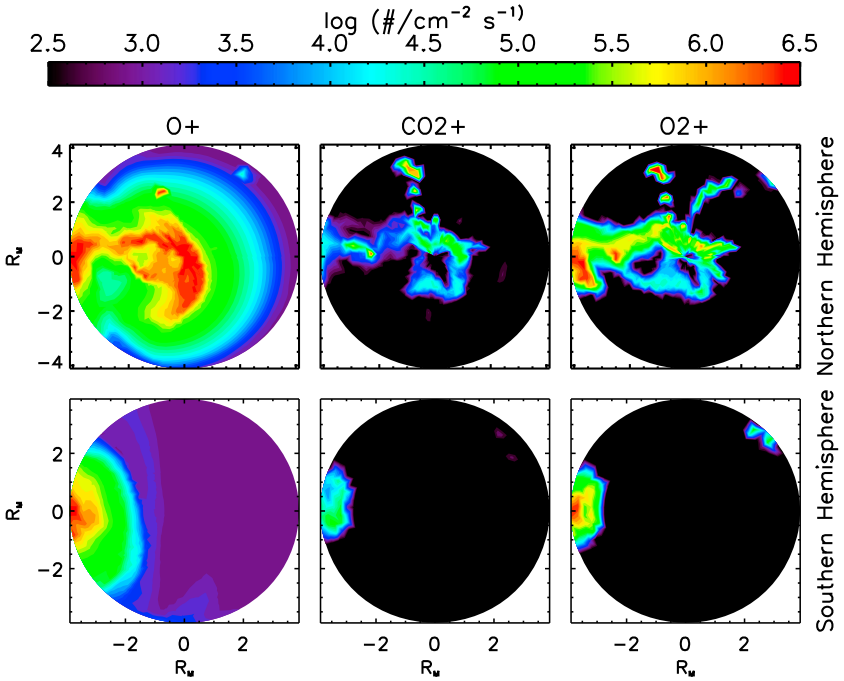

Figure 10. The escape of (left) O^+, (middle) CO_2^+ + (right) O_2^+ on a 4 R_M shell. The (top row) northern and (bottom row) southern hemisphere with the Sun to the right. The view for both hemispheres is from over the north pole and the color bar is in units of $cm^{-2}s^{-1}$.

roughly an order of magnitude greater than CO_2^+ at solar maximum and minimum. The efficiencies for loss are slightly higher at solar maximum, which is consistent with the findings of *Chaufray et al.* [2007].

During solar minimum, the O^+ outer loss is again 4 times larger than the heavy species but the ratio of the heavy species outer loss to O^+ loss is now 0.31, which is smaller than some of the recent observations: *Barabash et al.* [2007] found the loss ratio of heavies to O^+ to be 1.4 (for ASPERA-3 observations in 2006) with observations of O^+, CO_2^+, O_2^+ to be 1.6×10^{23}, 0.8×10^{23} and 1.5×10^{23}, respectively. Notice that our findings predict significantly more O^+ loss, which we determined was largely due to the low-energy (<10 eV) source, which an instrument may or may not see. A similar trend follows for ASPERA-3 observations from 2007 to 2011 by *Nilsson et al.* [2011] who found the loss ratio of heavies to O^+ to be 0.90 with observations of ($CO_2^+ + O_2^+$) and O^+ to be 9.5×10^{23} and 10.5×10^{23}, respectively. The study that most closely matched our predictions was by *Lundin et al.* [2009] who used ASPERA-3 observations from 2008 to 2009 and found that the loss ratio of heavies to O^+ to be 0.83 with observations of CO_2^+, O_2^+, and O^+ to be 0.35×10^{24}, 1.4×10^{24} and 2.1×10^{24}, respectively.

Figure 10 illustrates the spatial distribution of O^+, CO_2^+, and O_2^+ escape rates through a 4 R_M shell. The simulation domain uses a coordinate system that corresponds to MSO directions, and the escape shown is for an IMF with an away sector Parker spiral configuration. Figures 10 (top) and 10 (bottom) illustrate the northern and southern hemisphere loss shells, respectively. Note that the view is from over the north pole for all of the panels with the Sun to the right. The loss is calculated by recording a particle as it passes through the 4 R_M spherical shell and displayed in number flux, with the color bar on a log scale in # $cm^{-2}s^{-1}$.

The loss shells of O^+ in Figure 10 exhibit preferential loss in the northern polar plume and tail for the $+E_{SW}$ direction, which is in agreement with particle traces performed by *Fang et al.* [2008, 2010a] and *Curry et al.* [2013b]. As seen in the downtail detectors (Figures 5–6), the O^+ ions are accelerating with a slightly duskward flight direction and can be seen escaping on the 4 R_M shell with a plume starting at the pole and trailing down to the tail (a "mohawk" effect). This northern polar plume has been predicted in both MHD and hybrid models [*Modolo et al.*, 2005; *Brecht and Ledvina*, 2006; *Kallio et al.*, 2006, 2007; *Fang et al.*, 2008, 2010a; *Kallio et al.*, 2010; *Najib et al.*, 2011; *Curry et al.*, 2013b]. Interestingly, the CO_2^+ ions display a similar loss signature while the O_2^+ ions exhibit a predominantly tailward loss spatial signature. While VSDs from the magnetosheath are not presented here, all three species exhibit upward moving flight directions (θ <30°)

above 1 keV all throughout the sheath region. These acceleration ions in the sheath directly contribute to the escaping ions forming the plume.

4. Summary

Using the MTP simulation to create virtual detections of O^+, O_2^+, and CO_2^+ in an orbital configuration in the Mars space environment, we have presented results that highlight the dominant role of O^+ in ion escape at Mars. The energy-time spectrograms constructed from velocity space distributions for the different species around Mars showed the ion populations changing in energy and flux as the detector moves through the tail and sheath regions. In the tail, O^+ was observed by the virtual detectors at much broader energy ranges, 1 eV to 20 keV, while O_2^+ and CO_2^+ were confined to 1 eV to 1 keV. In the sheath, all species were observed above 1 keV but the O^+ flux dominated the virtual detections.

Focusing on two regions in the tail inside of the IMB, the VSDs exhibited markedly different signatures among the different species. Directly downtail, the virtual detectors observed high fluxes of duskward, low-energy O^+, much of which were produced in the corona at high altitudes. O_2^+ and CO_2^+ are not observed below ~7 eV here due to their cold neutral source of ions at lower altitudes, which were accelerated to ~10–700 eV downtail. Virtual detectors in the second region of interest near the southern pole observed high-energy, dawnward O^+ features in velocity space. While the low-energy O^+ was still present, the highly asymmetric beams of O^+ dominated the flux. Particle traces revealed that throughout the tail, O_2^+ and CO_2^+ do not exhibit the low- or high-energy VSD signatures due to their low-altitude cold planetary source of neutrals, as opposed to the hot extended oxygen corona that is ionized. In both cases, the IMF drove the duskward or dawnward asymmetries in flight direction. Future missions with both plasma and magnetometer instruments will be critical for assessing ion transport in near Mars space.

Finally, the escape of each species revealed particular spatial variations: O^+ dominates the polar plume while O_2^+ and CO_2^+ are more dominant in the tail. As seen in the energy-time spectrograms, much of the plume consists of high-energy accelerated ions from the $+z_{MSO}$ component of the convective electric field. Future work will include comparisons against data, particularly where in the tail and the sheath aligned with the convective electric field.

Acknowledgments

This work was funded by the NASA Goddard Space Flight Center under the Graduate Student Research Program (grant NNX10AL84H), by NASA grant NNX11AD80G, and NSF grant AST 0908311. The authors would also like to acknowledge Yuni Lee for her technical support.

Masaki Fujimoto thanks the reviewers for their assistance in evaluating this paper.

References

Acuna, M. H., et al. (1999), Global distribution of crustal magnetization discovered by the Mars global surveyor MAG/ER experiment, *Science*, *284*(5415), 790–793, doi:10.1126/science.284.5415.790.

Arkani-Hamed, J. (2001), A 50-degree spherical harmonic model of the magnetic field of Mars, *J. Geophys. Res.*, *106*, 197–208.

Barabash, S., and M. Holmstrom (2002), Energetic neutral atoms at Mars 4. Imaging of planetary oxygen, *J. Geophys. Res.*, *107*(A10), 1280, doi:10.1029/2001JA000326.

Barabash, S., A. Fedorov, R. Lundin, and J. A. Sauvaud (2007), Martian atmospheric erosion rates, *Science*, *315*(5811), 501–503, doi:10.1126/science.1134358.

Birdsall, C. K., and A. B. Langdon (1985), *Plasma Physics Via Computer Simulation*, 1st ed., McGraw-Hill, New York.

Bougher, S. W., and S. Engel (2000), Comparative terrestrial planet thermospheres: 3. Solar cycle variation of global structure and winds at solstices, *J. Geophys. Res.*, *105*, 669–692.

Bougher, S. W., S. Engel, D. Hinson, and J. Murphy (2004), MGS Radio Science electron density profiles: Interannual variability and implications for the Martian neutral atmosphere, *J. Geophys. Res.*, *109*, E03010, doi:10.1029/2003JE002154.

Bougher, S. W., J. M. Bell, J. R. Murphy, M. A. Lopez-Valverde, and P. G. Withers (2006), Polar warming in the Mars thermosphere: Seasonal variations owing to changing insolation and dust distributions, *Geophys. Res. Lett.*, *33*, L02203, doi:10.1029/2005GL024059.

Bougher, S. W., P. Blelly, M. Combi, J. L. Fox, I. Mueller-Wodarg, A. Ridley, and R. Roble (2008), Neutral upper atmosphere and ionosphere modeling, *Space Sci. Rev.*, *139*, 107–141.

Brecht, S. H., and S. A. Ledvina (2006), The solar wind interaction with the Martian ionosphere/atmosphere, *Space Sci. Rev.*, *126*(1-4), 15–38, doi:10.1007/s11214-006-9084-z.

Chaufray, J. Y., R. Modolo, F. Leblanc, G. Chanteur, R. E. Johnson, and J. G. Luhmann (2007), Mars solar wind interaction: Formation of the Martian corona and atmospheric loss to space, *J. Geophys. Res.*, *112*, E09009, doi:10.1029/2007JE002915.

Cipriani, F., F. Leblanc, and J. J. Berthelier (2007), Martian corona: Nonthermal sources of hot heavy species, *J. Geophys. Res.*, *112*, E07001, doi:10.1029/2006JE002818.

Cravens, T. E., J. U. Kozyra, A. Nagy, T. Gombosi, and M. Kurtz (1987), Electron impact ionization in the vicinity of comets, *J. Geophys. Res.*, *92*, 7341–7353.

Curry, S. M., M. Liemohn, X. Fang, D. Brain, and Y. Ma (2013a), Simulated kinetic effects of the corona and solar cycle on high altitude ion transport at Mars, *J. Geophys. Res. Space Physics*, *118*, 3700–3711, doi:10.1002/jgra.50358.

Curry, S. M., M. Liemohn, X. Fang, Y. Ma, and J. Espley (2013b), The influence of production mechanisms on pick-up ion loss at Mars, *J. Geophys. Res. Space Physics*, *118*, 554–569, doi:10.1029/2012JA.017665.

Dubinin, E., M. Fraenz, A. Fedorov, R. Lundin, N. Edberg, F. Duru, and O. Vaisberg (2011), Ion energization and escape on Mars and Venus, *Space Sci. Rev.*, *162*(1-4), 173–211, doi:10.1007/s11214-011-9831-7.

Ergun, R. E., L. Andersson, W. K. Peterson, D. Brain, G. T. Delory, D. L. Mitchell, R. P. Lin, and A. W. Yau (2006), Role of plasma waves in Mars' atmospheric loss, *Geophys. Res. Lett.*, *33*, L14103, doi:10.1029/2006GL025785.

Fang, X., M. W. Liemohn, A. F. Nagy, Y. Ma, D. L. De Zeeuw, J. U. Kozyra, and T. H. Zurbuchen (2008), Pickup oxygen ion velocity space and spatial distribution around Mars, *J. Geophys. Res.*, *113*, A02210, doi:10.1029/2007JA012736.

Fang, X., M. W. Liemohn, A. F. Nagy, J. G. Luhmann, and Y. Ma (2010a), On the effect of the Martian crustal magnetic field on atmospheric erosion, *Icarus*, *206*(1), 130–138, doi:10.1016/j.icarus.2009.01.012.

Fang, X., M. W. Liemohn, A. F. Nagy, J. G. Luhmann, and Y. Ma (2010b), Escape probability of Martian atmospheric ions: Controlling effects of the electromagnetic fields, *J. Geophys. Res.*, *115*, A04308, doi:10.1029/2009JA014929.

Fox, J. L. (2009), Morphology of the dayside ionosphere of Mars: Implications for ion outflows, *J. Geophys. Res.*, *114*, E12005, doi:10.1029/2009JE003432.

Fox, J. L., and A. Hac (1997), Spectrum of hot O at the exobases of the terrestrial planets, *J. Geophys. Res.*, *A11*, 24,005–24,011, doi:10.1029/97JA02089.

Fox, J. L., and K. Sung (2001), Solar activity variations of the Venus thermosphere/ionosphere, *J. Geophys. Res.*, *106*, 305–335.

Fraenz, M., et al. (2006), Plasma intrusion above Mars crustal fields—Mars Express ASPERA-3 observations, *Icarus*, *182*(2), 406–412, doi:10.1016/j.icarus.2005.11.016.

Hartle, R. E., M. Sarantos, and E. C. Sittler (2011), Pickup ion distributions from three-dimensional neutral exospheres, *J. Geophys. Res.*, *116*, A10101, doi:10.1029/2011JA016859.

Kallio, E. (2002), Ion escape from Mars in a quasi-neutral hybrid model, *J. Geophys. Res.*, *107*(A3), SIA1.1–SIA1.21, doi:10.1029/2001JA000090.

Kallio, E., A. Fedorov, E. Budnik, S. Barabash, R. Jarvinen, and P. Janhunen (2008), On the properties of O^+ and O_2^+ ions in a hybrid model and in Mars Express IMA/ASPERA-3 data: A case study, *Planet. Space Sci.*, *56*(9), 1204–1213, doi:10.1016/j.pss.2008.03.007.

Kallio, E., K. Liu, R. Jarvinen, V. Pohjola, and P. Janhunen (2010), Oxygen ion escape at Mars in a hybrid model: High energy and low energy ions, *Icarus*, *206*(1), 152–163, doi:10.1016/j.icarus.2009.05.015.

Kallio, E., et al. (2006), Ion escape at Mars: Comparison of a 3-D hybrid simulation with Mars Express IMA/ASPERA-3 measurements, *Icarus*, *182*(2), 350–359, doi:10.1016/j.icarus.2005.09.018.

Kallio, E., et al. (2007), Energisation of O^+ and O_2^+ ions at Mars: An analysis of a 3-D quasi-neutral hybrid model simulation, *Space Sci. Rev.*, *126*(1-4), 39–62, doi:10.1007/s11214-006-9120-z.

Kim, J., A. Nagy, J. L. Fox, and T. E. Cravens (1998), Solar cycle variability of hot oxygen atoms at Mars, *J. Geophys. Res.*, *103*, 339–342.

Leblanc, F., and R. E. Johnson (2002), Role of molecular species in pickup ion sputtering of the Martian atmosphere, *J. Geophys. Res.*, *107*(E2), 5010, doi:10.1029/2000JE001473.

Liemohn, M. W., S. M. Curry, X. Fang, and Y. Ma (2013), Comparison of high-altitude production and ionospheric outflow contributions to O^+ loss at Mars, *J. Geophys. Res. Space Physics*, *118*, 4093–4107, doi:10.1002/jgra.50388.

Luhmann, J. G., and J. U. Kozyra (1991), Dayside pickup oxygen ion precipitation at Venus and Mars spatial distributions energy deposition and consequences, *J. Geophys. Res.*, *96*, 5457–5467.

Luhmann, J. G., and K. Schwingenschuh (1990), A model of the energetic ion environment of Mars, *J. Geophys. Res.*, *95*(A2), 939–945, doi:10.1029/JA095iA02p00939.

Lundin, R., S. Barabash, M. Holmström, H. Nilsson, M. Yamauchi, E. M. Dubinin, and M. Fraenz (2009), Atmospheric origin of cold ion escape from Mars, *Geophys. Res. Lett.*, *36*, L17202, doi:10.1029/2009GL039341.

Lundin, R., S. Barabash, E. Dubinin, D. Winningham, and M. Yamauchi (2011a), Low-altitude acceleration of ionospheric ions at Mars, *Geophys. Res. Lett.*, *38*, L08108, doi:10.1029/2011GL047064.

Lundin, R., S. Barabash, M. Yamauchi, H. Nilsson, and D. Brain (2011b), On the relation between plasma escape and the Martian crustal magnetic field, *Geophys. Res. Lett.*, *38*, L02102, doi:10.1029/2010GL046019.

Ma, Y., A. Nagy, I. V. Sokolov, and K. C. Hansen (2004), Three-dimensional, multispecies, high spatial resolution mhd studies of the solar wind interaction with Mars, *J. Geophys. Res.*, *109*, A07211, doi:10.1029/2003JA010367.

Ma, Y.-J., and A. F. Nagy (2007), Ion escape fluxes from Mars, *Geophys. Res. Lett.*, *34*, L08201, doi:10.1029/2006GL029208.

Manning, C. V., Y. Ma, D. A. Brain, C. P. McKay, and K. J. Zahnle (2011), Parametric analysis of modeled ion escape from Mars, *Icarus*, *212*(1), 131–137, doi:10.1016/j.icarus.2010.11.028.

Martinis, C. R., J. K. Wilson, and M. Mendillo (2003), Modeling day-to-day ionospheric variability on Mars, *J. Geophys. Res.*, *108*(A10), 1383, doi:10.1029/2003JA009973.

Modolo, R., G. Chanteur, E. Dubinin, and A. Matthews (2005), Influence of the solar euv flux on the Martian plasma environment, *Ann. Geophys.*, *23*, 433–444.

Nagy, A., et al. (2004), The plasma environment of Mars, *Space Sci. Rev.*, *111*, 33–114.

Najib, D., A. F. Nagy, G. Tóth, and Y. Ma (2011), Three-dimensional, multifluid, high spatial resolution MHD model studies of the solar wind interaction with Mars, *J. Geophys. Res.*, *116*, A05204, doi:10.1029/2010JA016272.

Nilsson, H., N. J. T. Edberg, G. Stenberg, S. Barabash, M. Holmström, Y. Futaana, R. Lundin, and A. Fedorov (2011), Heavy ion escape from Mars, influence from solar wind conditions and crustal magnetic fields, *Icarus*, *215*(2), 475–484, doi:10.1016/j.icarus.2011.08.003.

Nilsson, H., G. Stenberg, S. Futaana, M. Holmstrom, S. Barabash, R. Lundin, N. Edberg, and A. Fedorov (2012), Ion distributions in the vicinity of Mars: Signatures of heating and acceleration processes, *Earth Planets Space*, *64*(2), 135–148, doi:10.5047/eps.2011.04.011.

Schunk, R., and A. Nagy (2000), *Ionospheres*, Cambridge Univ. Press, Cambridge, U. K.

Terada, N., Y. N. Kulikov, H. Lammer, H. I. Lichtenegger, T. Tanaka, H. Shinagawa, and T. Zhang (2009), Atmosphere and water loss from early Mars under extreme solar wind and extreme ultraviolet conditions, *Astrobiology*, *9*(1), 55–70, doi:10.1089/ast.2008.0250.

Valeille, A., M. R. Combi, S. W. Bougher, V. Tenishev, and A. F. Nagy (2009a), Three-dimensional study of Mars upper thermosphere/ionosphere and hot oxygen corona: 2. Solar cycle, seasonal variations, and evolution over history, *J. Geophys. Res.*, *114*, E11006, doi:10.1029/2009JE003389.

Valeille, A., V. Tenishev, S. W. Bougher, M. R. Combi, and A. F. Nagy (2009b), Three-dimensional study of Mars upper thermosphere/ionosphere and hot oxygen corona: 1. General description and results at equinox for solar low conditions, *J. Geophys. Res.*, *114*, E11005, doi:10.1029/2009JE003388.

Valeille, A., M. Combi, V. Tenishev, S. W. Bougher, and A. Nagy (2010), A study of suprathermal oxygen atoms in Mars upper thermosphere and exosphere over the range of limiting conditions, *Icarus*, *206*, 18–27, doi:10.1029/2005GL024059 10.1016/j.icarus.2008.08.018.

Yagi, M., F. Leblanc, J. Y. Chaufray, F. Gonzalez-Galindo, S. Hess, and R. Modolo (2012), Mars exospheric thermal and non-thermal components: Seasonal and local variations, *Icarus*, *221*(2), 682–693, doi:10.1016/j.icarus.2012.07.022.

Yamauchi, M., et al. (2007), IMF direction derived from cycloid-like ion distributions observed by Mars Express, *Space Sci. Rev.*, *126*(1-4), 239–266, doi:10.1007/s11214-006-9090-1.